Mon. Not. R. Astron. Soc. **284,** 981–993 (1997)

Formation of cavities in the X-ray emitting cluster gas of Cygnus A

David A. Clarke[1★], D. E. Harris[2★] and C. L. Carilli[2★†]

[1]*Department of Astronomy and Physics, Saint Mary's University, Halifax, NS, B3H 3C3, Canada*
[2]*Center for Astrophysics, 60 Garden Street, Cambridge, MA 02138, USA*

Accepted 1996 September 9. Received 1996 September 6; in original form 1996 July 1

ABSTRACT

The *ROSAT* data from the cluster gas of Cygnus A are re-examined in light of a three-dimensional hydrodynamic simulation of a supersonic jet propagating in an isothermal King atmosphere designed to follow the observed density distribution of the Cygnus A cluster gas. In addition to the presence of a non-uniform atmosphere, this simulation departs from previous 3D work in that the X-ray (bremsstrahlung) brightness distribution has been determined from the flow variables as a function of time. This simulation provides compelling evidence for the conclusions reached by Carilli et al. who stated that the major features of the X-ray brightness distribution are manifestations of the expanding lobe and the passage of a bow shock within the atmosphere. Further, this work demonstrates that these X-ray features are as much a function of the observing frequency and bandwidth as they are of the local conditions in the cluster gas of Cygnus A. In addition, new estimates of the Mach number of the jet ($M \gtrsim 4$) as well as the density and temperature jumps across the bow shock are derived by comparing the simulations with the X-ray data from Cygnus A.

Key words: hydrodynamics – galaxies: active – galaxies: individual: Cygnus A – galaxies: jets – X-rays: galaxies.

1 INTRODUCTION

Models for the hydrodynamic modification of the inter-cluster medium (ICM) by a supersonically expanding radio source were first presented by Blandford & Rees (1974) and Scheuer (1974) in the context of jet theory for powering the double radio emitting structures in extragalactic radio sources. These analytic models were followed by 2D numerical work (for example, Norman et al. 1982, Norman, Smarr & Winkler 1985, Clarke, Norman & Burns 1986, 1989, Lind et al. 1989 and Loken et al. 1992 among others) and, with the advent of large-memory supercomputers, 3D numerical work (Balsara & Norman 1992; Clarke 1993; Hardee & Clarke 1992, 1995). The 'standard model' emerging from these works is one in which expansion of the radio emitting structures is driven by the ram pressure of the jet and confined by the ram pressure of the ICM. At the jet terminus two shocks are formed: the jet-shock or Mach-disc which effectively stops the incoming jet, and the stand-off or bow shock which acts to accelerate and heat the external medium. The two shocked fluids (jet and ICM) meet in approximate pressure balance across a contact discontinuity (see Fig. 1). Observational evidence suggests that the contact discontinuity is largely stable to mixing (Carilli, Perley & Dreher 1988). Hence, the overall picture is one of a radio source being enveloped by a sheath of shocked ambient medium. If the jet direction is roughly constant over time, the radio lobe grows as a 'cigar-shaped' cavity, with the principal active surface being associated with the high radio surface brightness regions at the lobe extremities. The shocked ICM forms a thin, dense sheath in the vicinity of the radio hotspots (since this is the location of the driving 'piston'), and a broader, less-dense sheath between the radio lobe and the lateral side of the bow shock.

Cygnus A is by far the closest of the ultraluminous radio sources, and is considered the archetypical powerful radio galaxy. As such, Cygnus A has played a leading role in testing virtually all aspects of jet theory (see Carilli & Barthel 1996 and Carilli & Harris 1996 for reviews). The

★E-mail: dclarke@ap.stmarys.ca (DAC);
harris@head-cfa.harvard.edu (DEH);
ccarilli@aoc.nrao.edu (CLC)
†Present address: NRAO, PO Box 0, Socorro, NM 87801, USA.

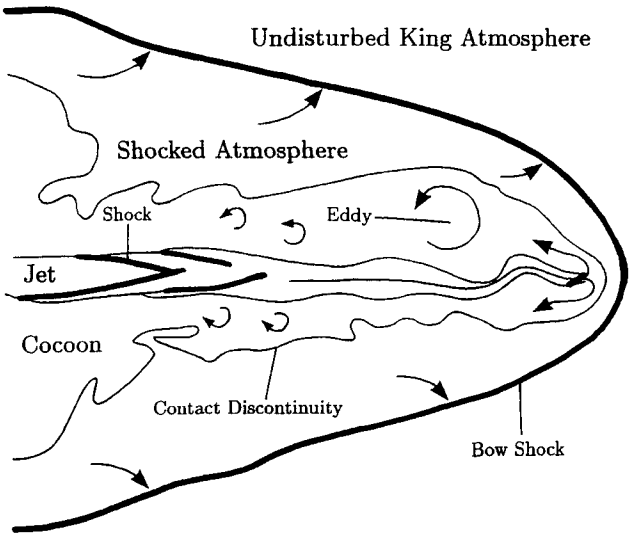

Figure 1. Anatomy of the jet simulation described in the text. The jet enters the grid through an orifice at the left boundary and at the centre of an isothermal King atmosphere. The major features are labelled.

ROSAT High Resolution Imager (HRI), with its improved sensitivity over previous X-ray telescopes, has precipitated a critical examination of the standard model and in particular, the interaction between an expanding radio source and the ICM. Carilli, Perley & Harris (1994; hereafter CPH) have recently presented *ROSAT* HRI observations of Cygnus A designed to search for signatures of the hydrodynamic modification of the cluster gas by the expanding radio source. They demonstrate that the X-ray surface brightness distribution in the vicinity of the radio source has been altered and in particular, find X-ray 'cavities' (relative to emission from the smoothed atmosphere) coincident with the coreward halves of the radio lobes and X-ray excesses coincident with the lobe edges. CPH interpret these features as evidence for the exclusion of thermal gas from the radio lobes, and emission from the displaced gas, respectively. While generally supporting the basic jet model for powerful radio sources, the physical analysis in CPH is necessarily limited and mostly qualitative since the expected X-ray surface brightness in the context of the 'standard model' is a rather complex function of the temperature and density in the unperturbed ICM and the shocked ICM, and of the energy response of the X-ray telescope. The principal difficulties are in estimating the strength of the bow shock, the width of the shocked sheath in the vicinity of the tails of the radio lobes, and the variation of density and temperature along the line of sight.

The problem of predicting the X-ray surface brightness for a cluster with an embedded radio source may be addressed by numerical simulations. Since the X-ray emissivity is a direct function of two hydrodynamic flow variables (namely density and temperature), it is a relatively straightforward task to compute the expected X-ray surface brightness from a 3D hydrodynamical simulation of a powerful radio source in a dense cluster. Herein, the results from such a computation (including a dynamically weak magnetic field) are presented. Emphasis is placed on predicting modifications to the X-ray surface brightness by the expansion of the radio source. Physically reasonable parameters for the cluster gas profile and for the radio jet are adopted, and the results are directly compared with a new *ROSAT* HRI image of Cygnus A including very recent additional observations. The relative role of local physical conditions to Cygnus A and the observing frequency/bandwidth is also discussed.

2 THE SIMULATION

2.1 Numerical methods

The simulation was performed using the 3D magnetohydrodynamic (MHD) code ZEUS-3D[1] as described in Clarke (1996a). This code uses recent innovations to maintain the stability and integrity of magnetic fields of any strength. It is an operator-split finite difference Eulerian scheme in which the multidimensional computations are performed using a combination of directional-split and planar-split steps. Interpolations are performed using the second-order upwinded, time-centred scheme described by van Leer (1977). A von Neumann–Richtmyer artificial viscosity (e.g., Richtmyer & Morton 1967) is used to stabilize shocks, which are typically resolved with three or four zones. The code has been extensively tested with test suites described in Clarke (1996a) and references therein.

The flow variables tracked during an MHD computation are the density, thermal energy density, three components of velocity and three components of the magnetic field. Visualizing these variables presents a challenge in and of itself, and the two methods used here are 2D slices (e.g., Fig. 2), and line-of-sight integrations (e.g., Fig. 3) through the data cube. The 2D slices are typically of the flow variables themselves (e.g., Fig. 2 depicts the density), but the line-of-sight integrations can depict interesting combinations of the variables such as the bremsstrahlung and synchrotron emissions (e.g., Fig. 3).

For this simulation, the thermal bremsstrahlung brightness f_x is derived by integrating the emissivity $[\varepsilon_x \propto n_e^2 (kT)^{-1/2} \, e^{-h\nu/kT}$, e.g., Tucker 1975] along the line of sight and over the effective sensitivity range of the *ROSAT* HRI, approximated here by a top-hat profile between 2.2×10^{17} and 4.1×10^{17} Hz, corresponding to photon energies of 0.9 and 1.7 keV respectively (CPH). The lower limit approximates the absorption cut-off of the Galactic medium ($n_H = 3 \times 10^{25}$ m^{-2}) while the upper cut-off represents the declining effective area of the *ROSAT* mirror. Thus,

$$f_x \propto \int_{los} n_e^2 (kT)^{1/2} (e^{-0.9/kT} - e^{-1.7/kT}) \, ds \qquad (1)$$

where n_e is the number density of electrons (taken as proportional to the fluid density). Any convenient prescription for scaling the variables may be used; in equation (1) the quantity kT is scaled in units of keV.

Although the simulation was performed assuming the lobes are dominated by hot, thermal matter, the salient results (i.e., the modifications to the X-ray surface brightness) are quite insensitive to whether the lobes are com-

[1]This is a code related to but distinct from the public domain code by the same name maintained by M. L. Norman at the National Center for Supercomputing Applications.

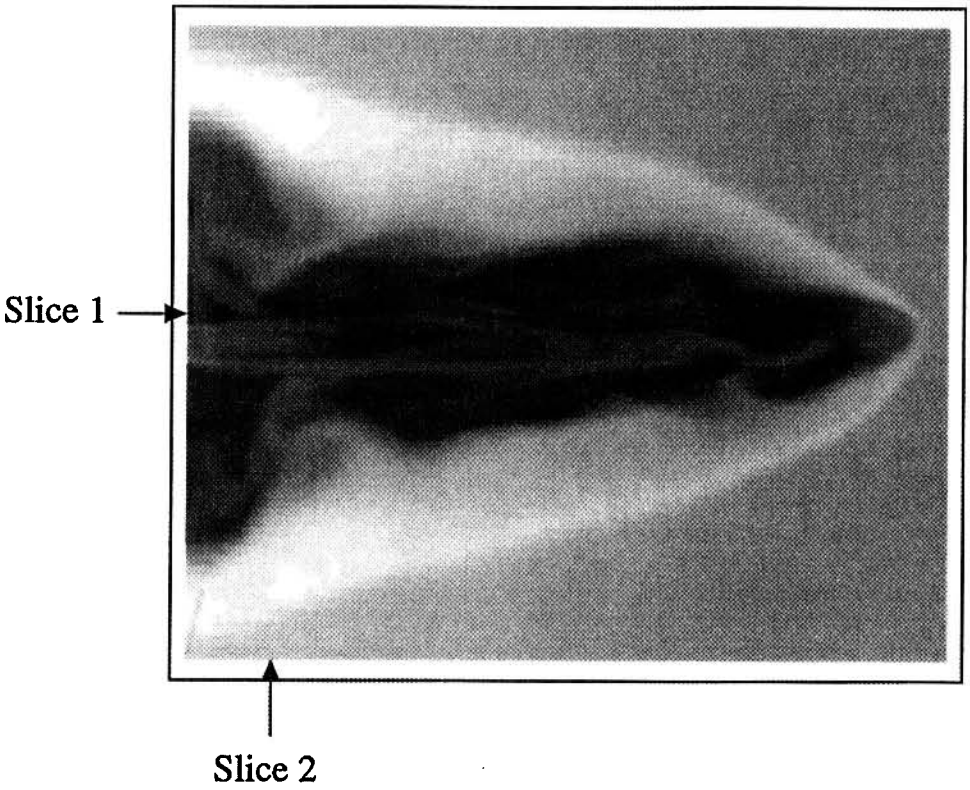

Figure 2. A 2D slice through the data cube at epoch $t=8$ depicting the density. The grey-scale ranges logarithmically from 0.0025 (black) to 2.5 (white) times the central density of the initial King atmosphere. Many of the features labelled in Fig. 1 can be identified. Locations of the 1D slices shown in Fig. 6 are indicated.

posed of thermal or relativistic plasma. All that is important is that the material in the lobes should not contribute in any significant way to the X-ray emission along the line of sight. This criterion is clearly satisfied whether the lobes consist of hot rarefied thermal plasma or a relativistic gas.

Finally, the synchrotron emission is computed using standard expressions for synchrotron emissivity (e.g., Longair 1981) and then assuming the relativistic particle number and energy densities are proportional to the density and pressure of the thermal fluid respectively. This is done because the relativistic particles are not tracked as independent entities. Note that such a prescription will reproduce the qualitative behaviour of the particles reasonably well. For example, at shocks where the thermal pressure increases, the energy density of the relativistic particles is also expected to increase (e.g., Fermi acceleration), etc. Further details may be found in Clarke et al. (1989).

2.2 Problem initialization

The simulation was initialized on a three-dimensional Cartesian grid with the 1-axis (i.e., the x coordinate) aligned along the initial jet axis. The 1-axis ranges from 0 to $50\,r_j$ (where r_j is the initial jet radius) and is resolved with 125 uniform zones ($0.4\,r_j$ per zone). Each transverse axis ranges from $-25\,r_j$ to $+25\,r_j$ and is resolved with 110 zones the dimension of which varies smoothly from $0.2\,r_j$ on the jet axis to slightly more than $0.8\,r_j$ at a distance $25\,r_j$ from the jet axis. In this way, higher numerical resolution can be attained along the jet axis where internal jet structures (e.g., shocks) are more sensitive to the grid spacing (see Fig. 1).

Two points must be made clear at this time. First, by most standards, this is a rather under-resolved jet with only a quarter of the resolution of most previous 2D simulations (e.g., Norman & Hardee 1988) and half the resolution of some recent 3D simulations (e.g., Hardee & Clarke 1995). Even so, this computation still required approximately 4 h of CPU and some 35 million words (280 Mbyte) of central memory on the Cray C-90 at the Pittsburgh Supercomputer Center. For the purpose of this work, the dynamics of the jet interior are not so critical, and only the displacement of the X-ray atmosphere by the inflating lobe is of concern here. For this, the resolution used in the simulation should be adequate.

Secondly, r_j refers to the jet radius in the *simulation* and not to the jet in Cygnus A itself. As powerful as modern computers may be, it is still impractical to attempt a simulation in which the cocoon attains a radius of $20\,r_j$ or more. Thus, the distance scale of the simulation is ultimately determined by the length of the lobe in the final epoch rather than the radius of the jet itself. In this simulation, the lobe attains a length of $\sim 47\,r_j$ (nearly the entire grid), and thus one jet radius in the simulation corresponds to ~ 1.5 arcsec (~ 1.5 kpc) in Cygnus A – roughly three times the *observationally measured* radius of the Cygnus A jet. Again, since discussion is limited to the inflation of the lobe within the X-ray atmosphere, this should be of little concern here.

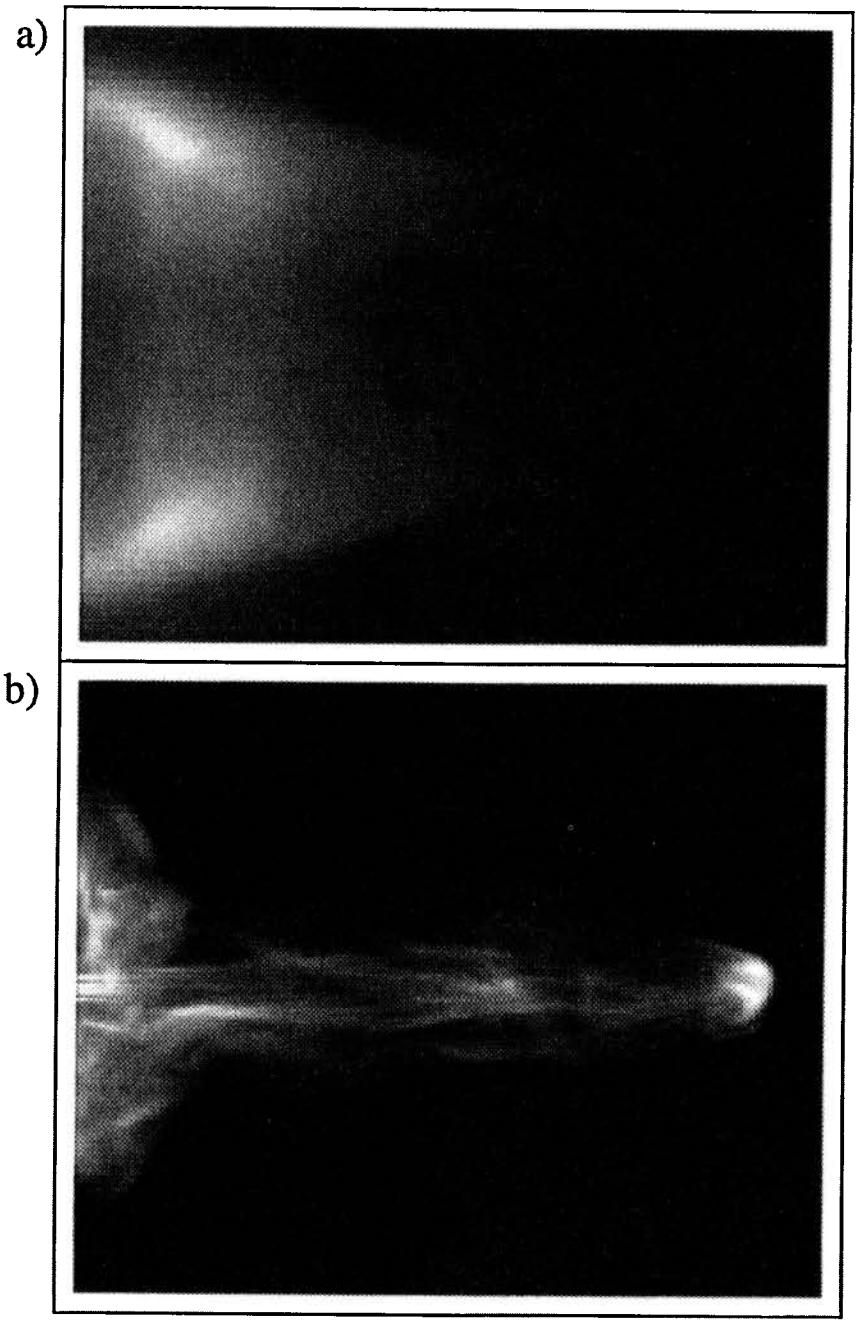

Figure 3. (a) Line-of-sight integration of the X-ray bremsstrahlung emissivity at epoch $t=8$. The dynamic range of the image (arbitrary units) is roughly 100 with bright X-ray regions depicted as white. The X-ray luminosity traces and atmosphere only – the density of the jet and lobe are too low to contribute significantly to the total brightness. Note the X-ray 'excesses' near the left-hand boundary where lines of sight pass exclusively through shocked ambient material. Conversely, an X-ray 'cavity' is produced near the jet orifice. (b) Line-of-sight integration of the synchrotron emissivity at epoch $t=8$. The dynamic range of the image is roughly 100 with bright regions depicted as white. The synchrotron emissivity traces the magnetized material confined to the jet and lobe.

Continuing with the details of the initialization, an isothermal ($T=4.76\times10^7$ K, $kT=4.1$ keV) King atmosphere was established throughout the grid (e.g., Forman & Jones 1991) centred on the grid origin:

$$n(r)=\frac{n_0}{[1+(r/a)^2]^{3\beta/2}} \qquad (2)$$

where n_0 is the central density (at $r=0$), a is the core radius, and β is the usual King model index (ratio of the mean velocity dispersion of the galaxies to the temperature of the gas, Gorenstein et al. 1978). For the Cygnus A environment, CPH report best fitting values of $n_0=(7.0\pm2.0)\times10^4$ m^{-3}, $a=35\pm5$ arcsec, and $\beta=0.75\pm0.25$. These values for the central density and temperature lead to a central pressure of $\sim4.6\times10^{-11}$ Pa and a sound speed of $\sim1.1\times10^6$ m s^{-1} throughout the atmosphere.

For the purpose of the calculation, the core radius a is taken to correspond to $22\,r_j$ from the grid origin. This is slightly less than half the extent of the grid in the 1-direction, corresponding to the observation that the core radius in the Cygnus A environment (35 arcsec) is about half the extent of the radio lobe. The density in the simulation is scaled to the observed central density. Thus, the initial density of the atmosphere at the grid origin is set to unity. Velocities are scaled to the sound speed in the unperturbed atmosphere, which is also set to unity. Thus, for a monatomic, non-relativistic gas ($\gamma=5/3$), the scaled central pressure is 0.6.

While providing a convenient fit, the isothermal King atmosphere is unphysical since it does not represent a system in hydrostatic equilibrium. The self-gravity from the matter distribution given by equation (2) does not balance the pressure gradients required by equation (2) and the ideal gas law for an isothermal gas. Thus, the atmosphere is artificially constrained to prevent it from expanding under its own pressure gradient before the jet has a chance to propagate through it. This is accomplished by imposing a 'pseudo-gravitational' potential ($\tilde{\phi}$) designed to 'hold on to' the atmosphere without significantly impeding the advancing jet. In practice, the form of the Euler equation normally solved by ZEUS-3D (Clarke 1996a) is modified to read:

$$\frac{\partial \boldsymbol{s}}{\partial t}+(\nabla\cdot\boldsymbol{v})\boldsymbol{s}=-\nabla(p-\rho\tilde{\phi})+(\boldsymbol{B}\cdot\nabla)\boldsymbol{B} \qquad (3)$$

where $\boldsymbol{s}$, $\boldsymbol{v}$, p, ρ, and $\boldsymbol{B}$ are the momentum per unit volume, velocity, thermal pressure, matter density, and magnetic induction (in units where $\mu_0=1$) respectively, and where $\tilde{\phi}$ is defined by

$$\tilde{\phi}\equiv\frac{p_K}{\rho_K}.$$

Here, p_K and ρ_K are the thermal pressure and matter density in the unperturbed King atmosphere respectively. Since this ratio is proportional to the temperature, $\tilde{\phi}$ is initially uniform throughout the atmosphere. By design, the quantity $\rho\tilde{\phi}$ exactly cancels the initial pressure gradients in the King atmosphere and thus, assuming no initial magnetic field, the right-hand side of equation (3) is zero. However, since the jet density is substantially less than that of the atmosphere, $p_j-\rho_j\tilde{\phi}\approx p_j$, and the pseudo-gravity has little effect on the jet dynamics.

A Mach 6 jet (i.e., the ratio of initial jet flow speed and jet sound speed) is launched into the atmosphere through an orifice ten zones in diameter centred on the origin of the grid located on the left-hand boundary of the 1-axis. The jet is given a density of 0.02 and is initially in pressure balance with the atmosphere at $r=0$. To break the azimuthal symmetry, the jet is wiggled at the orifice with a 2 per cent helical perturbation to the velocity. In addition, the jet transports a trace magnetic field so the synchrotron emissivity may be computed.

In the units defined in this subsection, a time interval of 1 in the simulation corresponds to $\sim 1.3\times10^6$ yr. The simulated jet reaches the end of the grid in a time $t\sim8.0$, corresponding to an overall age of $\sim10^7$ yr, which is consistent with ages usually assumed for FR II radio sources (10^7–10^8 years, Alexander & Leahy 1987).

2.3 Description of the calculation

Fig. 1 is a schematic of the calculation with some of the key features labelled. Figs 2 and 3 are representations of the jet, lobe, and ambient medium at $t=8$ in the units described in the previous subsection. Fig. 2 is a grey-scale image of density on a 2D slice that includes the jet axis. The features labelled in Fig. 1 can be seen clearly in this image. In particular, a bow shock separates the quiescent and shocked regions of the atmosphere, a contact discontinuity separates shocked atmosphere from shocked jet material filling the cocoon/lobe, and one or more 'jet-shocks' form the transition between the colder, collimated, supersonic jet to the hotter, chaotic, transonic cocoon. The 'walls' of the jet itself form, in essence, a contact discontinuity separating the jet and the cocoon. The inflation of the cocoon displaces ambient gas and the bow shock compresses it, thereby altering its X-ray emission.

While the jet is rarefied compared to the atmosphere, the density of the cocoon (filled with post-shock jet material) is more rarefied still. This may be counter-intuitive if one considers only the 1D shock jump conditions (e.g., Landau & Lifshitz 1959) in which post-shock material is always *compressed*. In multidimensions, however, material is compressed immediately downstream of the shock only. Thereafter, the high-pressure gas expands until pressure balance with the immediate surroundings (i.e., the jet and shocked ambient) is approximately restored. In this calculation, the expansion results in a cocoon 60 per cent hotter and 25 per cent less dense than the supersonic jet (see Table 1). As a consequence, even if the jet transports thermal protons, neither it nor the cocoon will contribute significantly to the observed X-ray brightness. Conversely, the energy density of relativistic particles and magnetic field is significantly higher in the jet and cocoon than in the ambient medium. Thus, the jet and cocoon are synchrotron-bright whereas the atmosphere is not. Fig. 3 illustrates these properties well. The bremsstrahlung image of Fig. 3(a) traces the atmosphere whereas the synchrotron image in Fig. 3(b) traces the jet and cocoon. Briefly, the synchrotron image shows a wealth of familiar structures, including filaments and a well-defined *double* hotspot, qualitatively similar to those found in the radio lobes of Cygnus A (Dreher, Carilli & Perley 1987). These features are described in Clarke (1996b) using a higher resolution simulation, and will be discussed in greater detail in a future paper.

Because the atmosphere is confined to the computational grid, the X-ray brightness image in Fig. 3(a) is incomplete – all the emission from the rest of the spherical distribution beyond the boundaries of the data cube is missing. To correct for this, Fig. 4 was generated by subtracting from Fig. 3(a) the emission of the initial atmosphere. The primary features in Fig. 4 include an emission 'cavity' in the middle of the widest part of the bow shock and two X-ray 'excesses' on either side of the cavity. The excesses are easy to understand. These are located along lines of sight which include mostly shocked (and compressed) ambient gas. In this calculation, the ambient gas in the vicinity of the X-ray excesses is approximately 1.6 times hotter and 2.2 times as dense as the unshocked ambient gas (Table 1). Thus, equation (1) implies the X-ray emissivity in the shocked ambient medium should be 4.3 times greater than that of the unperturbed

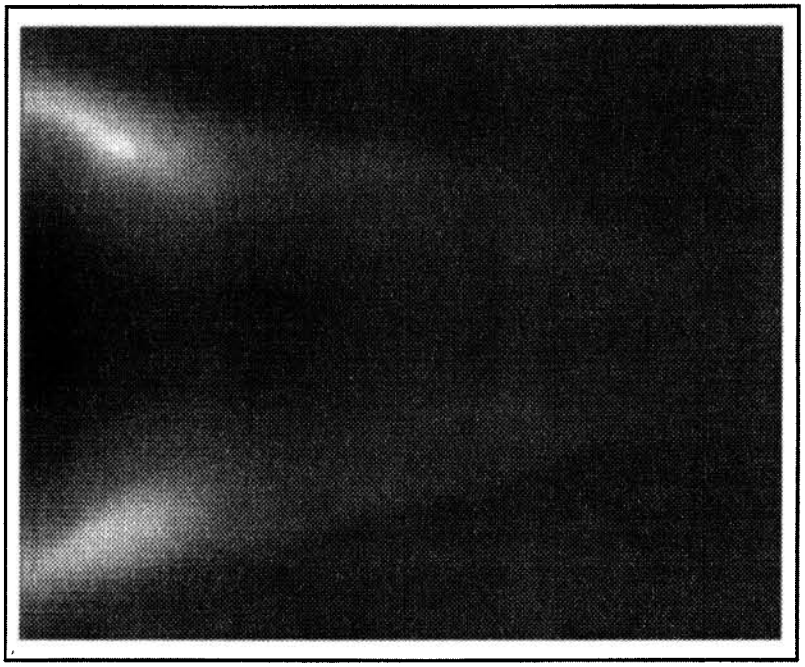

Figure 4. Same as Fig. 3(a), with the X-ray emissivity of the King atmosphere removed. In this representation, the X-ray excesses (white) and cavity (black) are particularly striking. In addition, the bow shock can be discerned. Note the residual X-ray brightness in much of the lobe interior is nearly zero, comparable to the unperturbed atmosphere.

Table 1. Densities, pressures, temperatures, and speeds from the simulation averaged over selected regions, relative to the central core values. Speeds are in units of the sound speed in the unperturbed atmosphere.

Region	ρ	p	T	v
central core	1.0	1.0	1.0	0.0
jet inlet	0.020	1.0	50.	42.
jet	0.0092	0.33	35.	39.
cocoon	0.0071	0.36	56.	4.9
shocked atmosphere	0.70	1.2	1.8	0.69
hot spot region only				
shocked atmosphere	0.30	2.9	9.3	2.8
quiescent atmosphere	0.14	0.14	1.0	0.0
x-ray excess region only				
shocked atmosphere	0.86	1.3	1.6	0.55
quiescent atmosphere	0.38	0.39	1.0	0.0

isothermal ($kT=4.1$ keV) King atmosphere, consistent with the bremsstrahlung emissivity 1D slice in Fig. 6(j).

On the other hand, the origin of the X-ray cavity may not be so obvious. While the reduced line of sight through the X-ray emitting material surely drives the brightness down, the enhanced density in the shocked ambient will drive the brightness up, and where these two effects balance warrants some investigation.

Consider equation (1) in the following form:

$$f_x \propto \int_{\rm los} n_{\rm e}^2 \mathscr{F}(kT)\,{\rm d}s, \tag{4}$$

where the function $\mathscr{F}(kT)$ contains all the temperature dependence in equation (1). In the vicinity of the initial temperature ($kT_0=4.1$ keV), $\mathscr{F}(kT)$ is a slowly *decreasing* function of kT for the observing frequency and bandwidth of the *ROSAT* HRI (Fig. 5).

Suppose now at the location of the X-ray cavity and excesses, the bow shock has expanded to a radius r from the jet axis and at this same location let the thickness of the shocked ambient medium (i.e., distance between the bow shock and contact discontinuity) be Δr. Let $n_{\rm e}$ and $n_{\rm e}'$ be the average electron density in the original atmosphere (within radius r) and in the shocked atmosphere (within the shell Δr) respectively. Let T and T' be the corresponding temperatures. Note that $n_{\rm e}<n_{\rm e}'$ and $T<T'$. Then, estimates of the X-ray brightness before (f_x) and after (f_x') the inflation of the lobe are

$$f_x \sim (n_{\rm e})^2 \mathscr{F}(kT) r \qquad f_x' \sim (n_{\rm e}')^2 \mathscr{F}(kT') \Delta r. \tag{5}$$

Note the different path lengths (r and Δr) used. Now, conservation of mass requires

$$\frac{n_{\rm e}'}{n_{\rm e}} = \frac{r^2}{\Delta r(2r-\Delta r)}. \tag{6}$$

In addition, for $kT=4.1$ keV (initial temperature of the isothermal King atmosphere) and $kT'=7.5$ keV (typical temperature in the shocked atmosphere in the simulation see Table 1), $\mathscr{F}(kT')/\mathscr{F}(kT)\sim 0.85$. Thus an estimate of the enhancement of X-ray brightness through the centre of the lobe is

$$\frac{f_x'}{f_x} \sim \frac{0.85}{\zeta(2-\zeta)^2}, \tag{7}$$

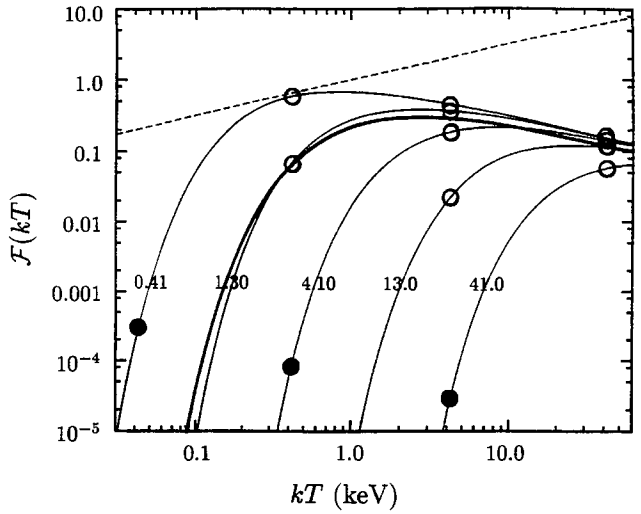

Figure 5. The temperature dependence of the bremsstrahlung emissivity [$\mathscr{F}(kT)$] integrated over the bandwidth of the *ROSAT* HRI (heavy line) plotted against the temperature (kT) of the gas. Note the weak dependence on temperature in the vicinity of $kT=4.1$ keV. The thinner lines show the temperature dependences of the emissivity for five hypothetical monochromatic detectors, representative of what will be available when high spatial resolution is coupled with adequate spectral resolution. The monochromatic frequencies are labelled with $h\nu$ (in units of keV) and are used to generate Fig. 8. Finally, the temperature dependence (dashed line) of an 'open bandwidth' (0.01 keV $\leq h\nu \leq$ 100 keV) is shown for comparison. As described in the text, the open and filled circles correspond respectively to the base-dominated and tip-dominated images in the parameter survey of Fig. 8.

where $\xi \equiv \Delta r/r$. For an X-ray deficit, f_x'/f_x must be less than unity, and thus expression (7) implies:

$$r \lesssim 3.4\Delta r \tag{8}$$

since, by definition, $\Delta r < r$. This is the condition for an X-ray deficit along the line of sight passing through the major axis of the radio lobe. Consequently, near the tip of the jet where the region of shocked ambient material is relatively thin ($r > 3.4\Delta r$), the X-ray brightness is enhanced. Conversely, far back from the tip of the jet where the shocked ambient region is relatively thick ($r < 3.4\Delta r$), the X-ray brightness is diminished and an X-ray 'cavity' results. The simplifications used here are justified by the simulation. The X-ray cavity is indeed roughly bounded by where inequality (8) holds true. Finally, one should note that the constant '3.4' depends upon the assumed value of the ratio $\mathscr{F}(kT')/\mathscr{F}(kT)$.

One-dimensional slices through the data cube reveal additional details of the structures found in the simulation. Fig. 6 depicts the density (ρ), pressure (p_1), temperature ($T = e_1/\rho$), velocity magnitude ($\|\boldsymbol{v}\|$), and bremsstrahlung emissivity (i_B) along a 1D slice parallel to the jet axis and through the double synchrotron hotspot (labelled 'slice 1' on Fig. 2), and along a 1D slice orthogonal to the jet axis and through the X-ray excesses (labelled 'slice 2' on Fig. 2). The units on the ordinates are as described in the previous subsection. Thus, for comparison between the simulation and Cygnus A, $(\rho, p_1, e_1/\rho, \|\boldsymbol{v}\|, i_B) = (1, 1, 1, 1, 1)$ on the plots correspond to $(7.00 \times 10^4$ m^{-3}, 7.66×10^{-11} Pa, 5.29×10^7 K, 1.15×10^6 m s^{-1}, 1.00×10^{-27} W m^{-3} Str^{-1}) in physical units. An interval of 1 on the abscissa corresponds to $\sim$1.5 kpc.

One can readily see the stronger jumps in the flow variables near the tip of the jet (Fig. 6a–d) than further back in the vicinity of the X-ray excesses (Fig. 6f–i), and this may be explained in terms of the relative strengths of the bow shocks at these locations. When the jet and ambient medium are in thermal pressure balance, one can show that the Mach number of the jet (M_j) and the Mach number of the advancing working surface in the ambient medium (M_{ws}) are related as follows (e.g., Loken et al. 1992):

$$M_{ws} = \frac{M_j}{1+\sqrt{\eta}} \tag{9}$$

where η is the ratio of jet and ambient densities ($\eta = 0.02$ at the jet orifice for this calculation). Thus, one could characterize the entire flow with a single 'jet Mach number' ($M_j = 6.0$), or by the effective Mach number of the working surface given by equation (9) ($M_{ws} \sim 5.3$). One may also define an effective 'local Mach number' at any point along the bow shock as the flow velocity (relative to the shock) divided by the local sound speed. At the tip of the bow shock, the local Mach number should be M_{ws}. Well back from the apex of the bow shock, the local Mach number will decrease and approach unity. The local Mach number can be estimated by considering the average temperature jump in the ambient medium across a given portion of the bow shock. From the 1D shock jump conditions, one can show that for a $\gamma = 5/3$ gas, the local Mach number is related to the temperature jump according to:

$$M^2 = \frac{8\tau - 7 + 4\sqrt{4\tau^2 - 7\tau + 4}}{5} \tag{10}$$

where τ is the ratio of upstream (shocked) to downstream (unshocked) temperatures. Thus, from the data in Table 1, the local Mach number near the tip of the jet is $\sim$5.2 (in good agreement with the estimate for M_{ws}), and through the X-ray excesses, $\sim$1.6. In the latter case, the obliquity of the bow shock (θ = the angle between the shock normal and the jet axis) has reduced the local Mach number by a factor $\cos\theta$, and thus $\theta \sim \cos^{-1}(1.6/5.2) \sim 72°$. This is consistent with the values measured directly from the simulation ($74 \pm 2°$).

In principle, one could extend this argument slightly and use the observed X-ray excess as an indicator of the local Mach number. Let r_s be the radius of the bow shock nearest the X-ray excess, and let r_x be the distance between the jet axis and the excess centroid. Then the line of sight through the X-ray excess is given by $2d = 2\sqrt{r_s^2 - r_x^2}$ (see Fig. 7). Now, if f_x is the observed X-ray brightness through the X-ray excess which, as in equation (4), depends weakly on temperature, then:

$$\frac{n_x}{n_0} \equiv \delta = \sqrt{\frac{f_x - 2f_\infty}{2f_0}} \tag{11}$$

where n_x is the average number density in the X-ray excess, n_0 is the average number density before the X-ray clump was shock compressed, and where f_∞ and f_0 are the X-ray brightnesses from the unshocked King atmosphere along the

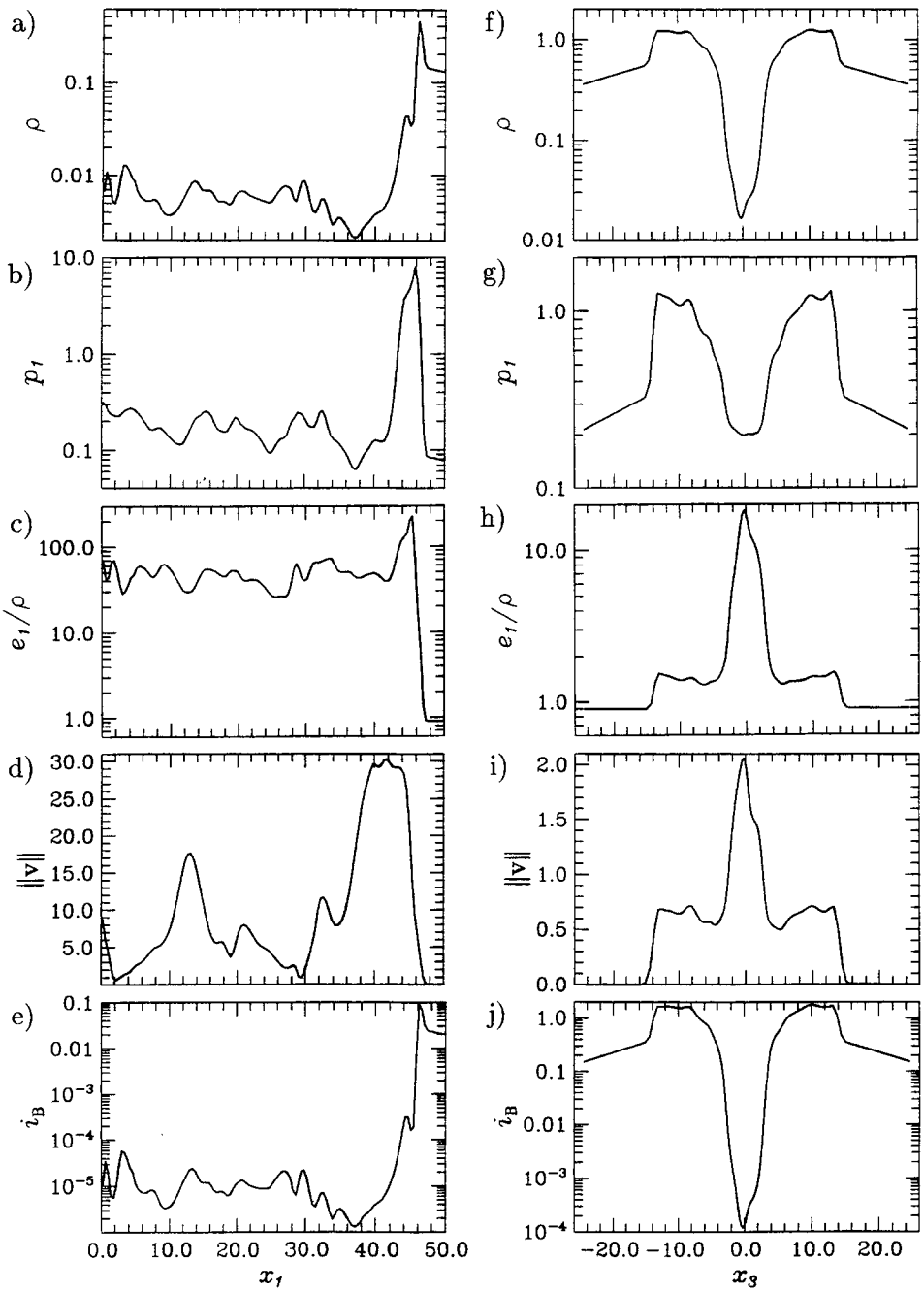

Figure 6. One-dimensional slices for (a) density (ρ), (b) pressure (p_1), (c) temperature ($T=e_1/\rho$), (d) speed ($\|v\|$), and (e) bremsstrahlung emissivity (i_B) along slice 1 (as labeled in Fig. 2), and (f)–(j) the same variables along slice 2. Slice 1 passes through the double synchrotron hotspot at the tip of the jet (Fig. 3b), while slice 2 passes through the X-ray excesses and cavity (Fig. 4). The conditions in the undisturbed King atmosphere can be seen in panels (a)–(e) for $x_1 > 47.5$, and in panels (f)–(j) for $|x_3| > 16.0$.

same line of sight as the X-ray excess integrated from d to ∞ and from 0 to d respectively. Then, from the shock jump conditions for a $\gamma = 5/3$ gas,

$$(M\cos\theta)^2 = \frac{3\delta}{4-\delta} \tag{12}$$

For example, from the simulation, $(f_x - 2f_\infty)/2f_0 \sim 2.8$. Thus, $\delta \sim 1.7$ and, for $\theta \sim 74°$, $M \sim 5.3$, comparable to previous measures of the Mach number of the working surface, namely 5.2 and 5.3. Note that the Mach number goes roughly as the fourth root of the X-ray brightness.

The X-ray properties of the simulation discussed in this section, including estimating an effective Mach number, will be applied to the X-ray observations of Cygnus A in Section 3.

2.4 Effects of observing frequency and temperature

Fig. 8 depicts 20 computed X-ray emission images (with the

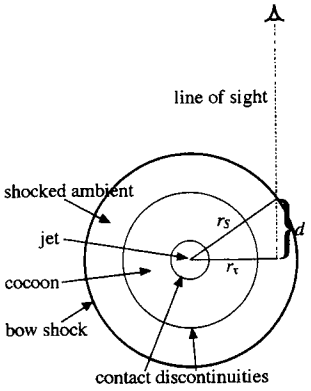

Figure 7. A schematic of a cross-section through the jet, lobe, and shocked atmosphere indicating the geometry for the emissivity integrations required for equation (11).

King atmosphere subtracted) for the simulation assuming four different atmospheric temperatures and five essentially monochromatic ($\Delta\nu/\nu \sim 10^{-4}$) observing frequencies. The temperature dependence of the bremsstrahlung emissivity for each frequency chosen in Fig. 8 is shown in Fig. 5, along with the temperature dependence for the *ROSAT* observations of Cygnus A and for an essentially open bandwidth ($0.01\ \mathrm{keV} \leq h\nu \leq 100\ \mathrm{keV}$).

Two distinct morphologies emerge from the parameter survey in Fig. 8. The 'tip-dominated' images found when $h\nu$ (where ν is the observing frequency) is significantly greater than kT (where T is the ambient gas temperature) are dominated by emission near the leading edge of the advancing bow shock, and bear little resemblance to Fig. 4. The X-ray excesses and cavity at the base of the cocoon discussed in the previous subsection are undetectable in these images. The filled circles in Fig. 5 correspond to three of the tip-dominated images in Fig. 8 – the remaining six (lower right of Fig. 8) are located well below the lower limit of the ordinate in Fig. 5. For these six cases, the X-ray emission from the shocked atmospheric gas is so weak (because of the exponential temperature dependence) that the structure displayed arises from the simulated jet and cocoon, not the atmosphere. It should be noted that in this simulation, the jet transports thermal matter only. If, in fact, the jet transports non-thermal (relativistic) matter exclusively, one would not expect to detect X-rays from the jet and cocoon, and all that might be observed is X-ray emission from the very apex of the bow shock.

The 'base-dominated' images comprise the second morphology and correspond to cases where $h\nu < kT$ (upper left of Fig. 8). These images correspond to the open circles in Fig. 5 where the temperature dependence is weak. Thus, density variations dominate the emission images and the X-ray cavity and excesses at the base of the radio source discussed previously (for example Fig. 4) are the predominant features.

Perhaps the more interesting images in Fig. 8 are those at or near the transition between the two morphologies. Base-dominated images close to the transition (e.g., $kT \sim 0.41$ keV, $h\nu \sim 1.30$ keV in Fig. 8) show the greatest contrast between the unshocked and shocked atmosphere. From images such as these, it may be possible to map the bow shock of the radio source directly. This will be discussed further in the next section.

Tip-dominated images close to the transition (e.g., $kT \sim 0.41$ keV, $h\nu \sim 4.10$ keV in Fig. 8) show the contact discontinuity between the cocoon and the shocked atmosphere. A contact discontinuity may also be described as a 'mixing layer' since it is here where the hot cocoon mixes with the dense atmosphere thereby rendering it visible at this frequency. Because such images effectively isolate the contact discontinuity from both the atmosphere and the radio lobe, it would be possible in principle to observe characteristics of the mixing layer directly (such as thickness, Kelvin-Helmholtz instabilities, entrainment, etc.). However, observing a contact discontinuity in this way may be difficult, if possible at all. For example, for Cygnus A ($kT = 4.1$ keV), one would have to observe at frequencies as high as $h\nu \sim 41$ keV ($\nu \sim 10^{19}$ Hz) and with a sensitivity at least five times greater than current *ROSAT* observations. Alternately, in order to observe this effect at *ROSAT* or *AXAF* bandwidths, one would have to observe a source a factor of 30 times cooler than Cygnus A (and with comparable number densities) and with a sensitivity at least 30 times greater than current *ROSAT* observations. Complicating this issue is whether the Cygnus A jet, or any active galactic nucleus jet for that matter, transports thermal protons. If not, it may be impossible to detect the contact discontinuity in this fashion. Indeed, this may prove to be a valuable observational discriminant to determine the nature of the matter in jets and lobes associated with extragalactic radio sources.

Because the *ROSAT* curve in Fig. 5 follows the monochromatic curve at $h\nu = 1.2$ keV very closely, images generated assuming a *ROSAT* bandwidth are virtually identical to those in Fig. 8 for $h\nu = 1.3$ keV (with the intensity levels scaled by the bandwidth ratio). For an open bandwidth, all images are base-dominated since the emissivity gently increases monotonically with temperature everywhere, and no features are significantly suppressed by modest temperature differences.

3 DISCUSSION

Fig. 9 shows the *ROSAT* image of Cygnus A with the contribution from the underlying (assumed) spherically symmetric isothermal King atmosphere subtracted. It is similar to Fig. 3 in CPH with additional data incorporated. Radio contours at 327 MHz are included for reference. As discussed by CPH, both lobes of Cygnus A show clear evidence of an X-ray cavity near the radio core. In addition, the eastern lobe shows two prominent X-ray excesses on either side of the cavity. The western lobe also shows evidence of the X-ray excesses, though the case is perhaps not so clear. Note the observed X-ray excesses at the tips of the lobes have been interpreted as evidence for synchrotron self-Compton emission (Harris, Carilli & Perley 1994) and are therefore not comparable to the tip-dominated morphology discussed in the previous subsection. In addition, the excess at the centre of the X-ray distribution is associated with the nucleus of the galaxy (Harris, Perley & Carilli 1996). Evidently, there is strong qualitative agreement between the calculations and the observations: the X-ray image of Cygnus A has a base-dominated morphology as expected

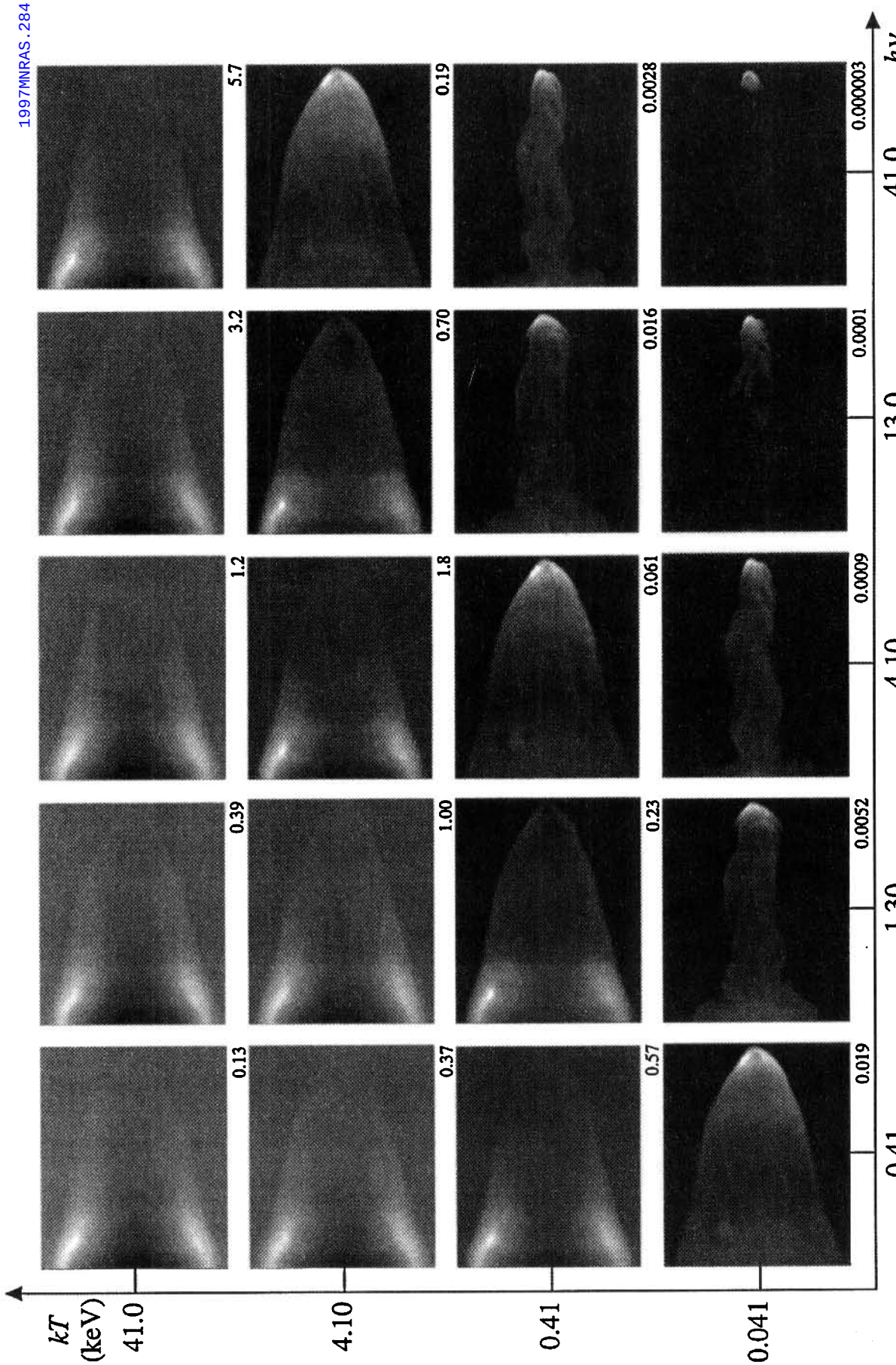

Figure 8. Line-of-sight integrations of the X-ray brightness of the simulation for various source temperatures and monochromatic observing frequencies with the contribution from the isothermal King atmosphere removed. The value of the brightest pixel, normalized to the brightest pixel on the frame at $h\nu = 1.30, kT = 4.10$ (corresponding roughly with Fig. 4), is given under the lower right corner of each frame. When $h\nu \lesssim kT$ (panels to the upper left), the X-ray emission is dominated by the widest portion of the sheath between the lobe and bow shock ('base-dominated'). Conversely, when $h\nu > kT$ (lower right), the emission is dominated by the strongly shocked gas with the largest temperature increase ('tip-dominated'). Note that the X-ray emission from the jet and lobe in some of the tip-dominated images (e.g., the panel at $h\nu = 13.0$ keV, $kT = 0.41$ keV) may not be physically meaningful because it originates from thermal gas used to model these structures in the simulation. Whereas, many radio source models posit that the actual pressure within the jet and lobe is dominated by relativistic plasma. The dynamic ranges of the images are 1000 and 100 for the tip-dominated and base-dominated images respectively.

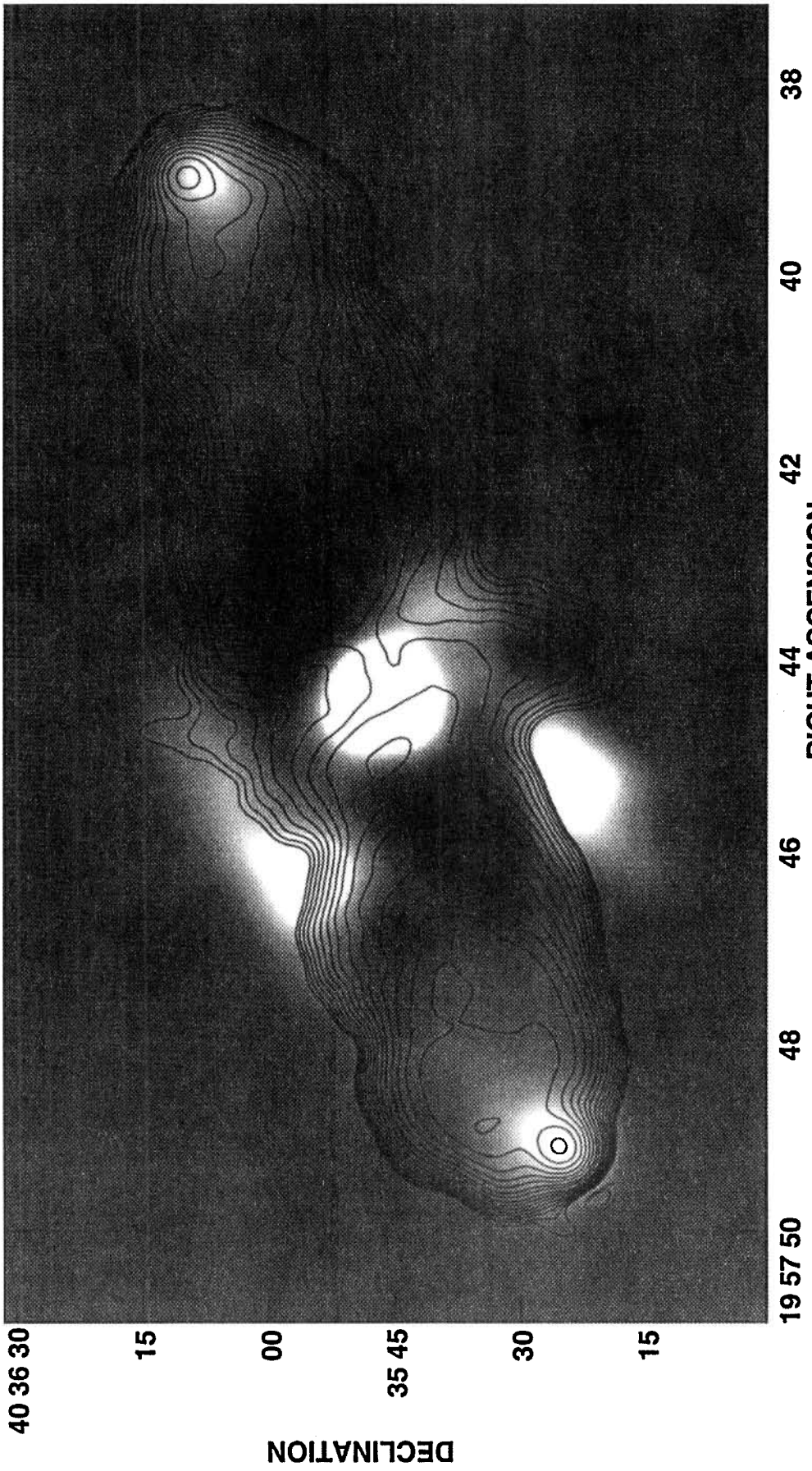

Figure 9. A grey-scale representation of the residual X-ray emission from the *ROSAT* observations (135 ks) of Cygnus A after a smoothed cluster surface brightness distribution (isothermal King atmosphere) has been subtracted. White denotes an excess of X-ray emission relative to the cluster atmosphere while black denotes an X-ray deficit. The bright spots corresponding to the radio hotspots are from synchrotron self-Compton X-rays (Harris et al. 1994), and are not accounted for in these simulations. 327-MHz radio contours are included for reference.

from the known atmosphere temperature and the observing bandwidth.

In light of the discussion in the previous section, a more detailed comparison between the observations and the simulation may be made. First, the X-ray cavities evidently correspond to the region where the thickness of the shocked ambient medium is more than ~25 per cent the distance between the jet axis and the bow shock [expression (8)]. Secondly from the X-ray data, one finds $f_x/2f_0 \sim 2.8$ and $f_\infty/f_0 \sim 0.7$.[2] Thus, from equation (11), $\delta \sim 1.4$, and from equation (12), $M\cos\theta \sim 1.3$. Thirdly, if the X-ray excesses are a result of shocked ambient material near the bow shock, then the angle θ can be estimated directly from Fig. 9. One then finds $\theta \gtrsim 70°$, and thus $M \gtrsim 4$. Strictly speaking, this is the Mach number of the working surface of the jet (M_{ws}). However, for a *very* light jet ($\eta \lesssim 10^{-6}$ is required to develop a lobe as extended as observed in Cygnus A), equation (9) implies M may be viewed as the Mach number of the jet (M_j) or the working surface (M_{ws}). Finally, note that while $M\cos\theta$ is insensitive to the observables, M itself is very sensitive to θ, particularly as θ approaches 90°. Thus, for example, if θ were as high as 85°, $M \sim 15$.

However, in units of the surface brightness of the central core of the King atmosphere, the total surface brightness of the X-ray excesses in the simulation and in Cygnus A is about 1.06 and 0.96 respectively. This would argue for a slightly *lower* Mach number in Cygnus A than for the simulation (in which $M_j = 6$). This is contrary to the suspicion that jet Mach numbers of 10–20 are required if a jet is to remain stable for 50 to 100 jet radii, as seems to be the case for Cygnus A (Clarke 1996b, and references therein). This intriguing discrepancy may be evidence that the actual jet is three or four times *wider* than the diameter inferred from the radio images, as suggested for independent reasons by Rudnick & Katz-Stone (1996).

Finally, the entire bow shock excited by the expansion of the lobes into the atmosphere is clearly seen in Fig. 4 but difficult to detect in Fig. 9. This may be for a variety of reasons. The data may be too noisy to pick out the subtle contrasts observed across the bow shock in Fig. 4, the bow shock may be relatively weak particularly if the Mach number is as little as 4, the atmosphere is probably clumpy, etc. Future *AXAF* observations may help in this area. Fig. 10 shows computed X-ray images of the simulation (again, with the King atmosphere removed) using three of the anticipated *AXAF* bandwidths (i.e., 1–3, 3–5 and 5–7 keV). The basic features in Fig. 4 are all intact (i.e., the cavity and excesses), though some subtle yet important differences are apparent. For example, at higher frequencies the contrast across the bow shock increases – a trend clearly seen in Fig. 8 as well. This is because at the higher energies, the ambient gas emissivity is falling exponentially whereas the shocked gas surrounding the cocoon will be well matched to the bandpass (e.g., Fig. 10c). Further, since the angular resolution for *AXAF* is anticipated to be an order of magnitude better than that of *ROSAT*, it should be possible to map the bow shock in unprecedented detail.

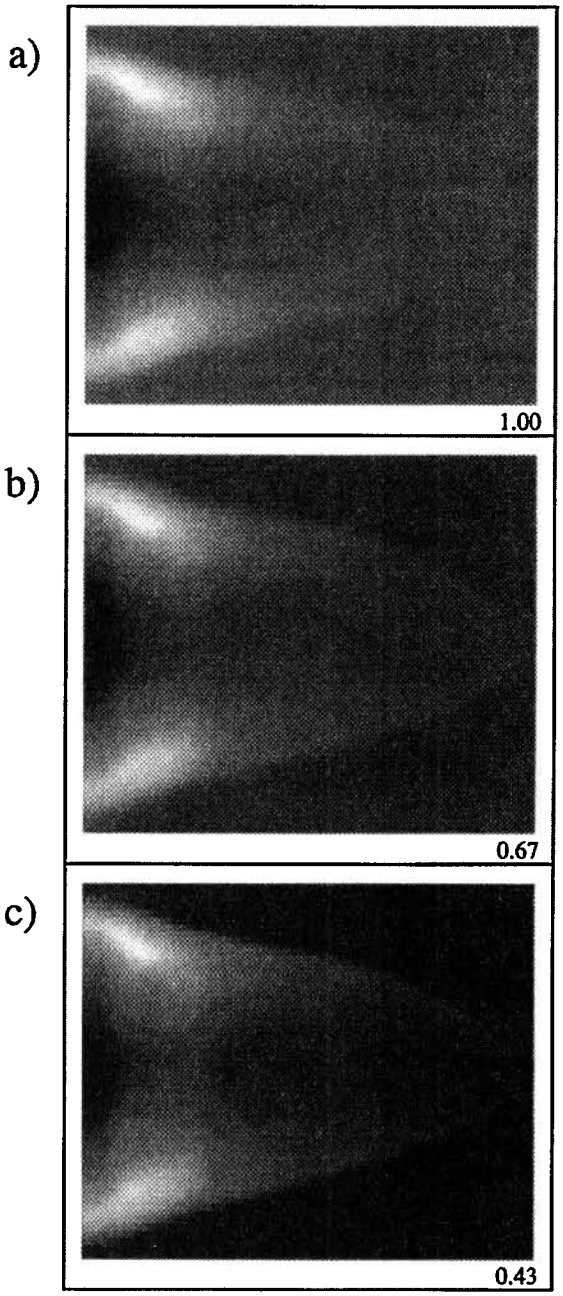

Figure 10. Line-of-sight integrations of the X-ray luminosity of the simulation (with the contribution from the isothermal King atmosphere removed) assuming the inferred temperature of the Cygnus A atmosphere ($kT = 4.1$ keV) at three anticipated *AXAF* bandwidths: (a) 1–3 keV, (b) 3–5 keV, and (c) 5–7 keV. While all images are base-dominated, the contrast of X-ray emission across the bow shock increases with increasing observing frequency. The numbers under the lower right corner of each frame indicate the brightest pixel relative to the brightest pixel in the 1–3 keV frame.

4 CONCLUSIONS

A three-dimensional hydrodynamical simulation has been performed to model the inflation of the Cygnus A radio

[2]Note that according to the definitions of f_0 and f_∞ in Section 2.3, $2f_0 + 2f_\infty$ is the total surface brightness of the unperturbed King atmosphere at the location of the X-ray excesses. Evaluating this is straight forward but estimating f_0 and f_∞ separately is a bit more difficult and one relies to some extent on the simulations for this. Fortunately, $M\cos\theta$ itself is rather insensitive to these values.

lobes within the cluster atmosphere as determined from X-ray observations. Good qualitative agreement is found between the simulated X-ray images and *ROSAT* data. It is demonstrated how the radio jet and lobe evacuate a cavity in the ambient hot gas and how the compressed gas between the bow shock and the radio lobe produces X-ray bright features. In short, this calculation supports the earlier contention of CPH that the X-ray observations of Cygnus A are a direct confirmation of the Blandford & Rees (1974) model for the development and evolution of extragalactic radio sources.

Quantitative comparisons are made between observed and simulated parameters. These show that the *ROSAT* data of Cygnus A are consistent with a moderate Mach number for the jet ($M \gtrsim 4$) and correspondingly moderate density and temperature jumps at the working surface and in the vicinity of the X-ray excesses (Table 1).

The X-ray appearance of a Cygnus A-like source at other observing frequencies and for a range of ambient gas temperatures are generated. These simulated images show how the observable X-ray features undergo dramatic changes between cases where the X-ray brightness is dominated by the density and cases where temperature changes are the determining factors. It is shown that future X-ray observations, particularly at higher frequencies, should be able to image the bow shock surrounding the radio lobes of Cygnus A. Such an observation would be unprecedented for extragalactic radio sources.

ACKNOWLEDGMENTS

We thank Rick Perley for discussions at the beginning stages of this project, and David Lane of Saint Mary's University for help with the figures. DAC acknowledges the support of an operating grant and an equipment grant from the Natural Sciences and Engineering Research Council of Canada (NSERC). DEH acknowledges support from NASA grants NAG5-1537 and NAG5-30934. The simulations were performed on the Cray C-90 at the Pittsburgh Supercomputer Center through grant AST930015P.

REFERENCES

Alexander P., Leahy J. P., 1987, MNRAS, 225, 1
Balsara D., Norman M. L., 1992, ApJ, 393, 631
Blandford R., Rees M., 1974, MNRAS, 165, 395
Carilli C. L., Barthel P. D., 1996, Astronomy and Astrophysics Review Series, 7, 1
Carilli C. L., Harris D. E., 1996, Proc. Greenbank Workshop, Cygnus A – Study of a Radio Galaxy. Cambridge Univ. Press, Cambridge
Carilli C. L., Perley R. A., Dreher J. W., 1988, ApJ, 334, L73
Carilli C. L., Perley R. A., Harris D. E., 1994, MNRAS, 270, 173 (CPH)
Clarke D. A., 1993, in Röser H.-J., Meisenheimer K., eds, Proc. Second Ringberg Castle Workshop, Jets in Extragalactic Radio Sources. Springer, Berlin, p. 243
Clarke D. A., 1996a, ApJ, 457, 291
Clarke D. A., 1996b, in Hardee P. E., Zensus A., Bridle A. H., eds, ASP Conf. Ser. Vol. 100, Workshop on Energy Transport in Radio Galaxies and Quasars. Astron. Soc. Pac., San Francisco, p. 311
Clarke D. A., Norman M. L., Burns J. O., 1986, ApJ, 311, L63
Clarke D. A., Norman M. L., Burns J. O., 1989, ApJ, 342, 200
Dreher J. W., Carilli C. L., Perley R. A., 1987, ApJ, 316, 611
Forman W., Jones C., 1991, in Fabian A., ed., Clusters and Superclusters of Galaxies. Kluwer, Dordrecht, p. 49
Gorenstein P., Fabricant D., Topka K., Harnden F. R., Jr, 1978, ApJ, 224, 718
Hardee P. E., Clarke D. A., 1992, ApJ, 400, L9
Hardee P. E., Clarke D. A., 1995, ApJ, 451, L25
Harris D. E., Carilli C. L., Perley R. A., 1994, Nat., 367, 713
Harris D. E., Perley R. A., Carilli C. L., 1996, in Ward M. J., O'Brien P., guest eds, Proc. Oxford Torus Workshop. Vistas Astron., 40, 45
Landau L. D., Lifshitz E. M., 1959, Fluid Mechanics. Pergamon Press, Oxford
Lind K. R., Payne D. G., Meier D., Blandford R. D., 1989, ApJ, 344, 89
Loken C., Burns J. O., Clarke D. A., Norman M. L., 1992, ApJ, 392, 54
Longair M. S., 1981, High Energy Astrophysics. Cambridge Univ. Press, Cambridge
Norman M. L., Hardee P. E., 1988, ApJ, 334, 80
Norman M. L., Smarr L., Winkler K.-H. A., 1985, in Centrella J., LeBlanc J., Bowers R., eds, Numerical Astrophysics. Jones and Bartlett, Boston, p. 88
Norman M. L., Smarr L., Winkler K.-H. A., Smith M. D., 1982, A&A, 113, 285
Richtmyer R. D., Morton K. W., 1967, Difference Methods for Initial-Value Problems, 2nd edn. Wiley Interscience, New York
Rudnick L., Katz-Stone D., 1996, in Carilli C. L., Harris D. E., eds, Proc. Greenbank Workshop, Cygnus A Study of a Radio Galaxy. Cambridge Univ. Press, Cambridge, p. 158
Scheuer P. A. G., 1974, MNRAS, 166, 153
Tucker W. H., 1975, Radiation Processes in Astrophysics. MIT Press, Cambridge
van Leer B., 1977, J. Comp. Phys., 23, 276